Science Advances
AAAS

advances.sciencemag.org/cgi/content/full/6/46/eabc6800/DC1

Supplementary Materials for

Multilayer fabrication of durable catheter-deployable soft robotic sensor arrays for efficient left atrial mapping

Varun Kashyap, Alexandre Caprio, Tejas Doshi, Sun-Joo Jang, Christopher F. Liu, Bobak Mosadegh*, Simon Dunham*

*Corresponding author. Email: sid2012@med.cornell.edu (S.D.); bom2008@med.cornell.edu (B.M.)

Published 13 November 2020, *Sci. Adv.* **6**, eabc6800 (2020)
DOI: 10.1126/sciadv.abc6800

The PDF file includes:

Other Supplementary Material for this manuscript includes the following:

(available at advances.sciencemag.org/cgi/content/full/6/46/eabc6800/DC1)

Supplementary Information

Fabrication of SRSA

The soft robotic sensor arrays (SRSA) presented in this work are composed of individual bending actuators that utilize pleats between individual segments to allow for low pressure, thin form factor actuators, similar to those described in prior works on soft robotics undertaken by our research group(*20–22*, *27*). Earlier work focused on design and optimization of soft actuator cages that could be used for this type of application, with a focus on evaluating a range of actuator geometries and assessing which possess optimal conformability. However, these designs did not incorporate sensors or address the intrinsic challenges of implementing a large number of sensors over the surface of a soft balloon. The focus of this work is on designs and processes that allow for a fully functional integrated sensor array on a soft actuator cage.

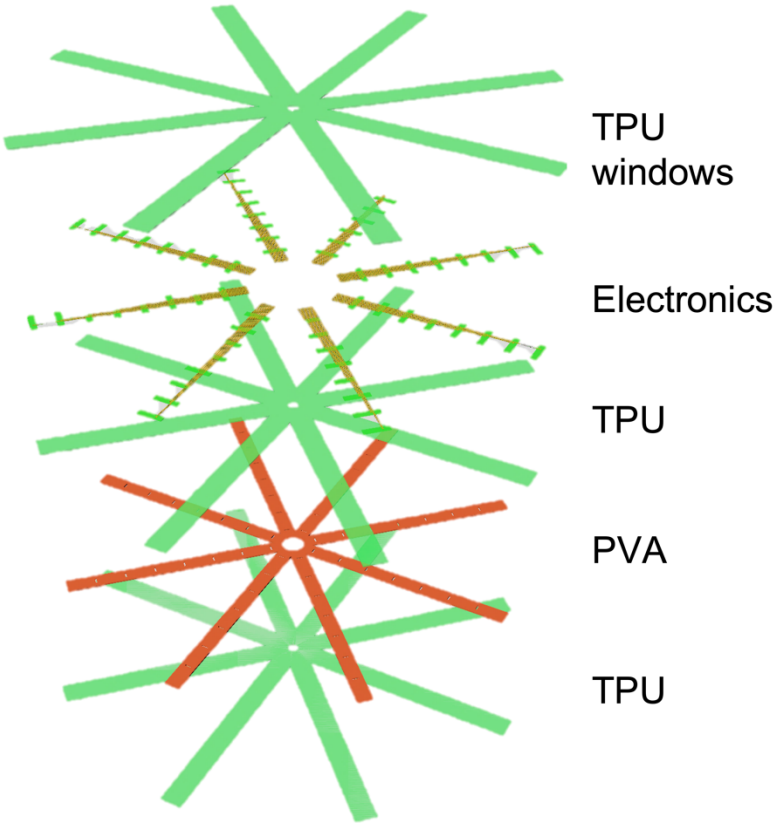

Figure S1. Fabrication stack up for soft robotic sensor array (SRSA). Each layer plays a pivotal role in the overall performance of SRSA.

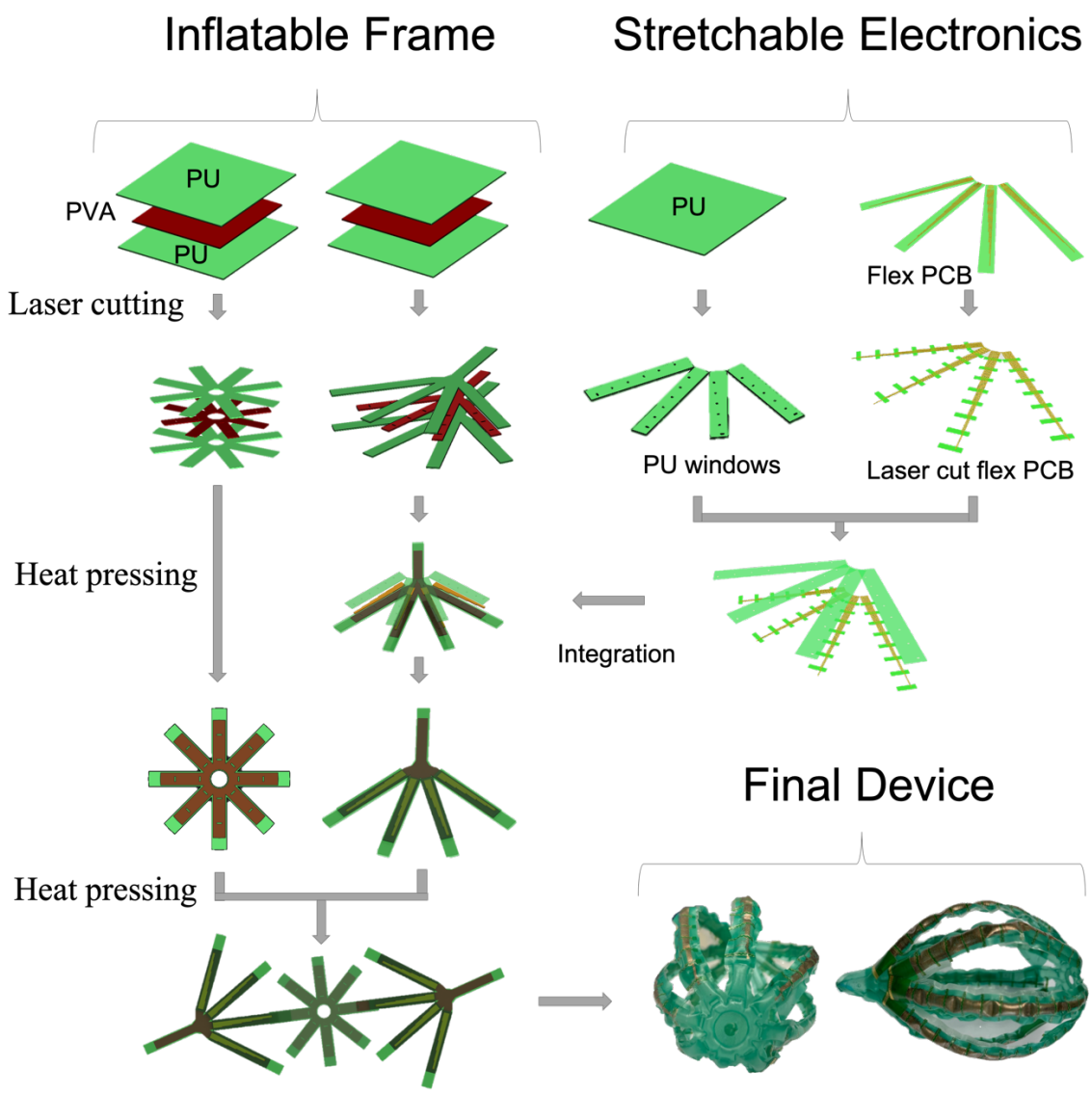

Figure S2. Steps for the fabrication of soft robotic sensor array (SRSA) for left atrium experiments. The multi-step fabrication process includes separate fabrication of hub and legs (inflatable frame), the stretchable electronics and their integration to produce the final device (SRSA). Photo Credit: Alexandre Caprio, Weill Cornell medicine

Left atrium conformability experiments

In order to mimick the mechanical properties of the left atrial tissue, Tango-plus was used as our 3D print material as discussed in earlier works(*23–26*). This choice of material was based on the properties and anatomic structure being replicated which is mainly in the noncalcified anatomic region. Elastic property of Tango-plus material is expressed by its young's modulus (ratio of stress to strain) which has a manufacturer reported value of 0.146 MPa at 20% strain.

Catheter deploy-ability of SRSA

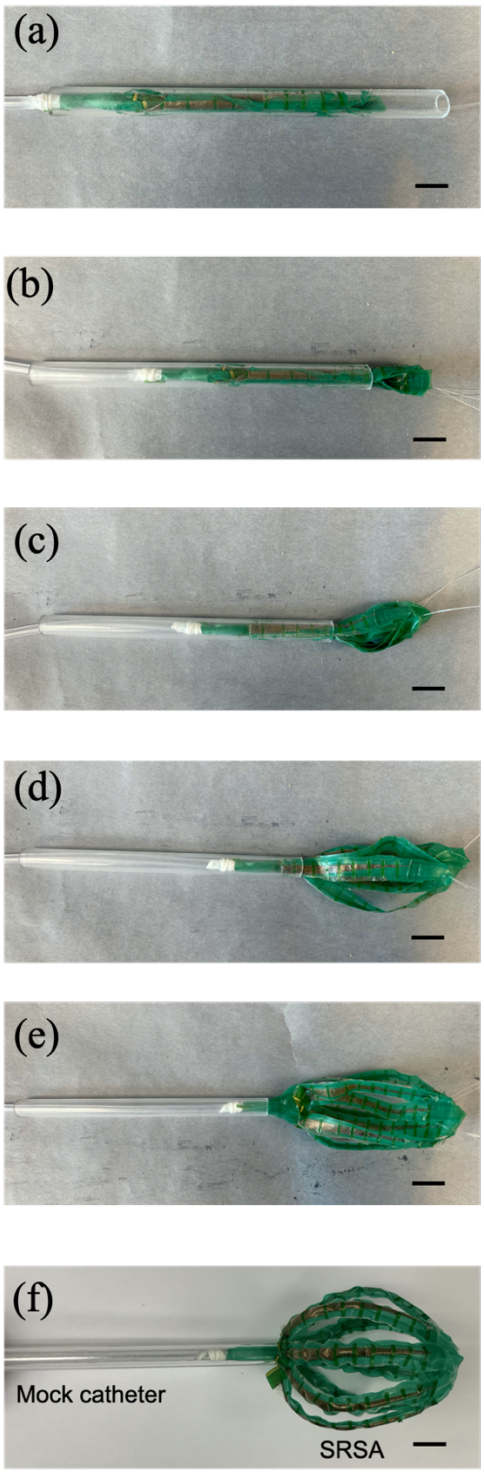

Figure S3. SRSA deployed from a 13.5 Fr mock catheter. Scale bar is 1 cm. Photo Credit: Alexandre Caprio, Weill Cornell medicine

Flex-PCB layer thickness

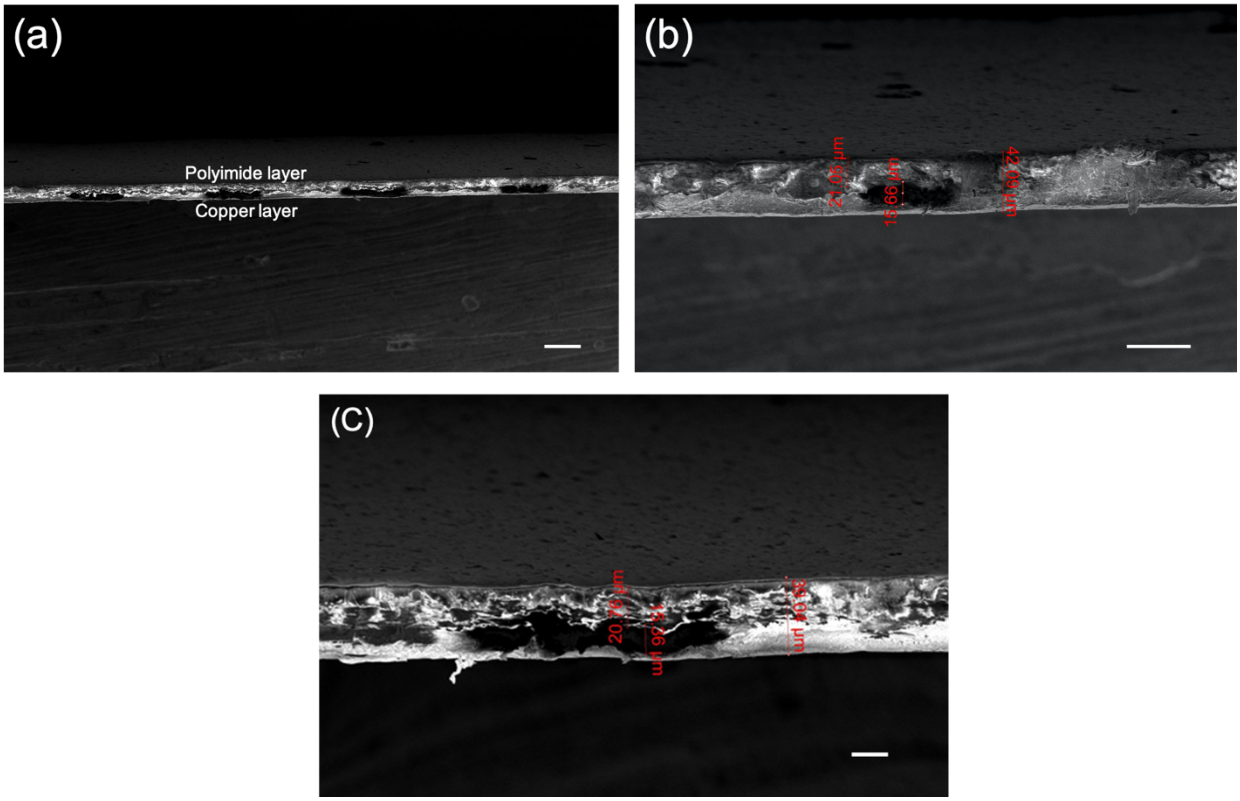

Figure S4. End on SEM images of Flex-PCB before postprocessing. (a) Scale bar is 100 µm (b) Scale bar is 50 µm. (c) Scale bar is 20 µm

Flex-PCB design

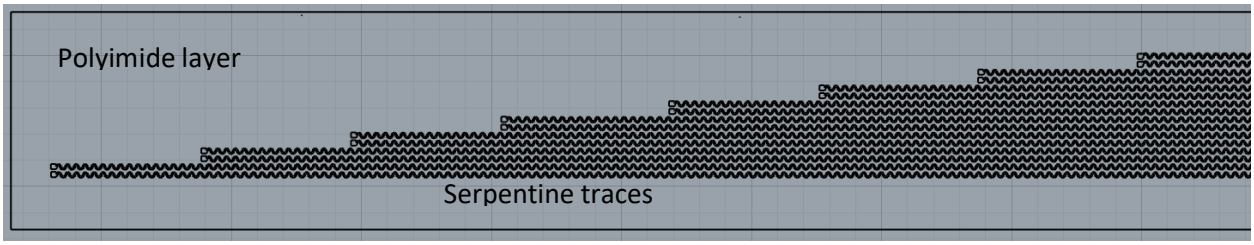

Figure S5. Design of Flex-PCB. The design consists of 16 electrodes, copper serpentine traces and polyimide layers for insulation.

Various key aspects were considered while designing the Flex-PCB for this application. The dimensional limitations of the flex house were accounted for while trying to accommodate maximum number of sensors for efficient mapping within the left atrium. Gonzalez et al (*36*) studied three different serpentine patterns and regions of highest plastic strain concentration were identified. In order to avoid the high stress concentration, a high radius of curvature is preferred and therefore a horseshoe design is recommended in this study. In another study by Van der Sluis et al (*37*), triangular serpentine patterns are compared against horseshoe patterns and a lower stress concentration is observed in the latter.

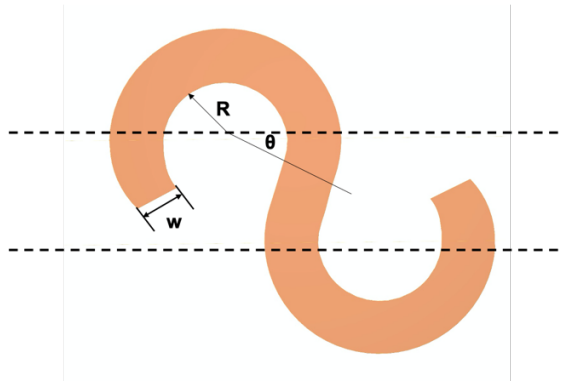

Figure S6. Key parameters for stretch-ability.

Key parameters that affect stretch-ability and stress concentration include inner radius, R, joining angle, q and width of the trace, w as shown in Figure S6. It is shown that for a given youngs modulus, and scale factor (R/w), equivalent plastic strain is lower for the Semicircle design which is a modification of the horseshoe design with q = 0°. Therefore, this configuration was chosen to be used in our study. High value of R or increasing amplitude reduces the accumulated strain. However, since the width of the soft actuator is fixed, the total number of traces and hence the total number of sensors is a function of amplitude of individual traces. Furthermore, the lowest possible spacing between traces possible by the flex house was 3 mil (~0.07mm). These

dimensions were used as the limits in our design. Low trace width is desired in order to achieve further strain reduction. This parameter was chosen based on the dimensional limitations of the flex house which was about 2 mil (~0.05mm). Based on this, our trace width is ~0.06mm.

Zhang et al (*38*) showed another parameter responsible for the stretch-ability of traces. A representative unit cell of a serpentine interconnect consists of two half circles, and two straight lines with the length l2 and spacing l1 as shown in Figure S7.

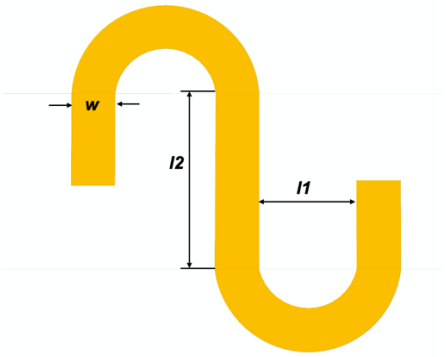

Figure S7. Representative unit cell of serpentine interconnect.

Here, the ratio of l1 and l2 is defined as a. This ratio (length/spacing) has an influence on the elastic stretch-ability of the serpentines. It is shown that the elastic stretch-ability reaches a maximum value at a = 1 and plateaus. In our design, a (~0.67) was optimized to obtain maximum stretch-ability and low strain.

FEA Analysis

The FEA analysis was performed using the static structural module on ANSYS workbench. Individual traces after the postprocessing step were modelled on TPU layer. Thicknesses obtained from the SEM images were used in this model. Note that maximum deformation occurs at the pockets and hence this region was considered in the simulations. The pockets are part of the linear actuator design applied here, that allow for low strain actuation(*20*). They are formed by patterning the sacrificial PVA layer in a manner to allow the TPU to fuse in regions of the actuators such that it subsequently inflates in discrete pockets. Materials including polyimide for the insulation, copper for the traces and polyurethane for the underlying layer were defined and relevant material properties were used. A hyperplastic model was defined and the relevant constants were used as shown in our earlier work(*20*). The pockets are constrained on both ends as described earlier. Therefore, these boundary conditions were defined in the model. A pressure of 10 PSI was applied for actuation. The strain and maximum deformation were plotted as shown in Figure 3 of the manuscript.

Tensile test

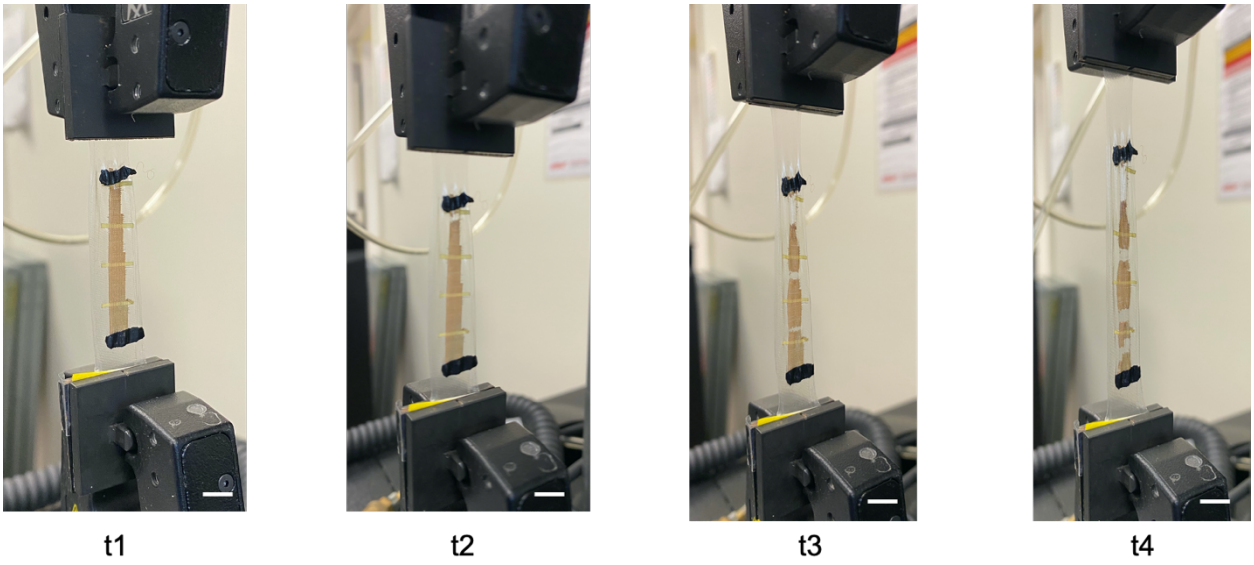

Figure S8. Tensile test on stretchable sensor array. Scale bar is 1 cm. Photo Credit: Varun Kashyap, Weill Cornell Medicine

Tensile test was conducted (Instron universal testing system) between flex-PCB and stretchable sensor array to determine their stretchability. First, the flex-PCB was mounted between tensile test grips. An increasing load was applied as a function of time and the corresponding extension was documented. A sudden dip is seen at the point of failure and the breakage of the traces can also be inspected visually. The corresponding strain at the point of failure was found to be ~0.9%. Next, stretchable sensor arrays (after post processing) were encapsulated in a transparent TPU as the substrate and subjected to tensile test as shown in Figure S8. We acknowledge that the failure point of the electrical traces is different from that of the substrate. Here the substrate (TPU) was gripped as shown in the figure. We believe this best represents the configuration of the SRSA when deployed and actuated within the left atrium. Here, the strain was observed to be ~30% at the first point of failure (t2, figure S8) as shown in figure 2g of the manuscript.

Table S1: Number of sensors in contact

Atrium	Number of sensors establishing near field sensing (>2mm)	Number of sensors that fall near the feature (mitral valve and pulmonary veins)	Number of sensors that do not make near field contact
1	94	28	6
2	78	38	12
3	102	18	8
4	78	24	26

Sensor characterization

In vitro voltage mapping evaluations were performed on a single array of sensors (16 sensors, associated with a single actuator leg) using a cardiac tissue phantom. This Gelatine based phantom was synthesized using a method suggested by Owda et al (*39*), which is designed to provide tissue-like electromagnetic and mechanical properties. A function generator provided pulsed waveforms to the phantom with a range of frequencies, pulse widths, and amplitudes meant to encompass values typical for cardiac electrograms to the tissue phantom(*40*, *41*). The SRSA was placed in contact with the phantom and signals were measured with the sensor (via an oscilliscope) at different distances from the phantom surface both in saline (distances ranging from 0.5mm to 2mm) and dry conditions. The distances were controlled by placing 3D printed spacers of varied

thicknesses between the sensor electrodes and phantom atrial tissue. The schematic of the setup is shown below.

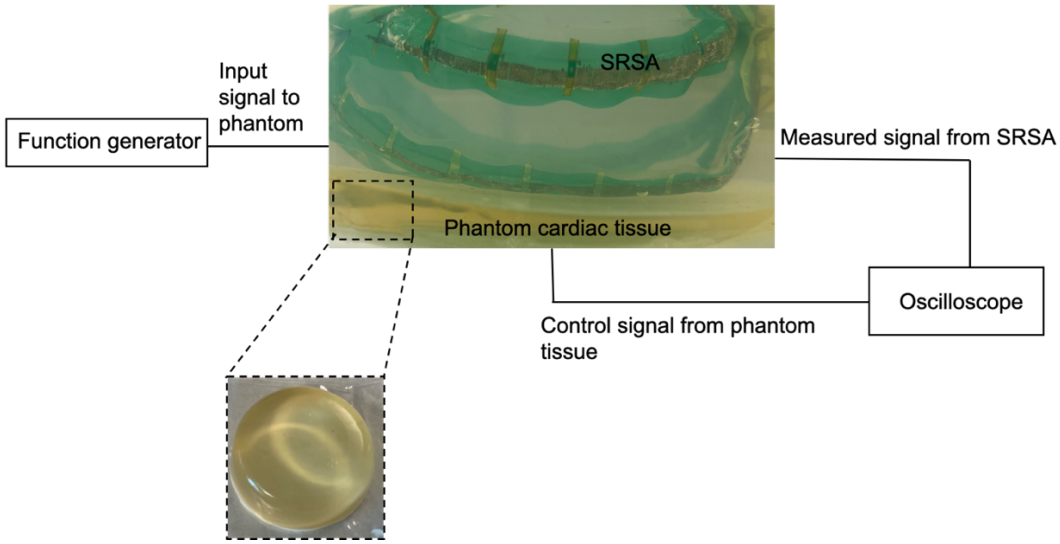

Figure S9. Schematic of system to measure mock waveforms on a phantom atrial tissue. A mock waveform with physiologically relevant voltage amplitudes and frequencies is passed through the phantom cardiac tissue using a function generator and the signal from SRSA sensors is measured using a oscilloscope. Photo credit: Varun Kashyap, Weill Cornell medicine.

Baseline measurements from the phantom were compared with the waveforms measured by SRSA sensors at the same location on the phantom tissue. An oscilloscope was used to obtain simultaneous measurements and compared. Ability of the sensors to resolve individual features of the wave was characterized. For a frequency of 1Hz, the amplitude was varied between 2mV and 1V and pulse width between 20ms and 300ms. As highlighted by Zanon et al(*40*), these parameters are comparable to that of a realistic electrogram. Figure S10 shows the ability of SRSA to resolve the signal in this range of pulse widths for the above-mentioned voltages. In addition, we observed that the sensors exhibit excellent temporal fidelity. Figure S11 shows the representative sensor data from SRSA for low voltage (2mV) and low pulse width (50ms) in phosphate buffered saline (PBS) for near field sensing (between 0.5mm and 2mm). This demonstrates the sensors ability to read electrograms effectively.

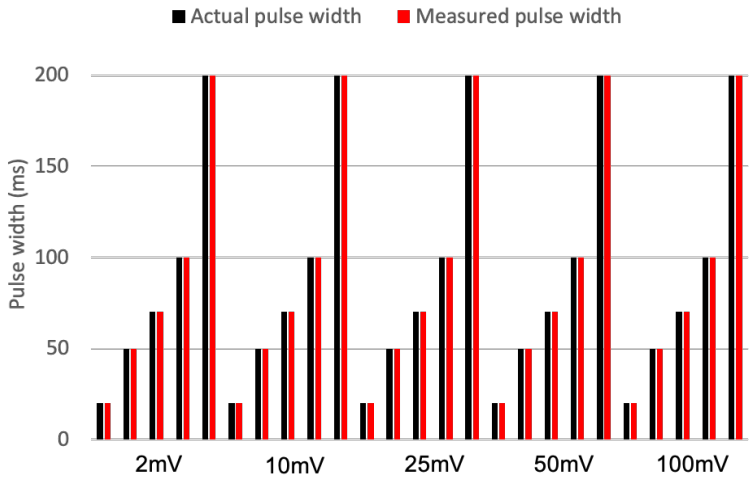

Figure S10. Schematic of system to measure mock waveforms on a phantom atrial tissue

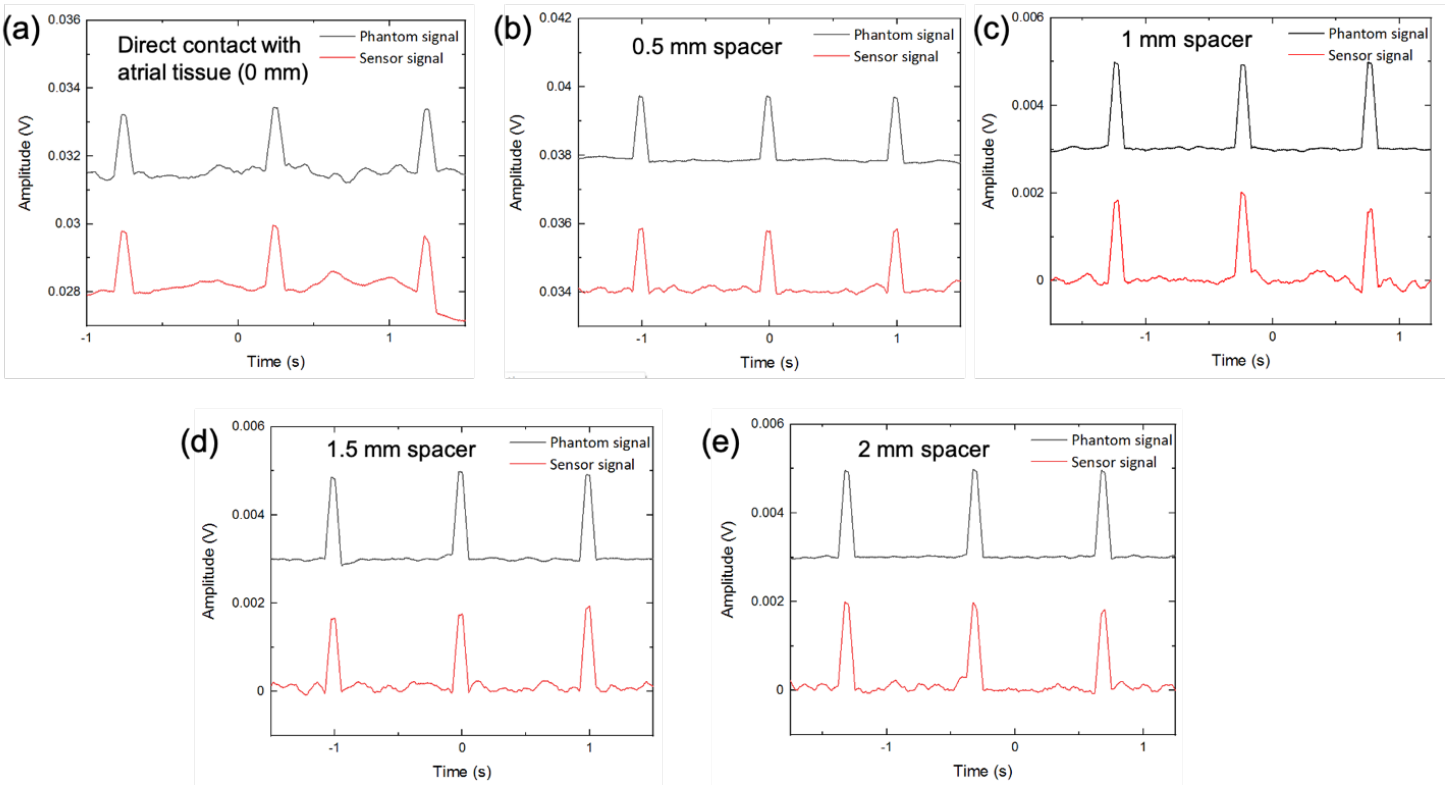

Figure S11. Input waveforms and measured waveforms using sensors on SRSA for near field contact (upto 2mm). The input waveform has a voltage of 2mV and pulse width of 50ms.

Excised porcine cadaver flow loop experiment

To address the dynamic motion of the device, we deployed it in the left atria of an excised porcine cadaver (unfixed tissue) and utilized a pulsatile flow loop (Shelley Medical) to produce realistic flow and deformations (*42*). An excised porcine heart was connected to the pulsatile flow pump as shown in Figure S12. The pump was set to a flow rate of 100 mL/s and a frequency of 0.5-1 Hz. SRSA was inserted into the left atrium from the right atrium through the transseptal puncture. The ventricle was trimmed to allow observed using an endoscope through the mitral valve (the microCT used for the static evaluations does not possess sufficient temporal resolution for use in dynamic pulsatile experiments). These videos are provided as supplementary videos 1 and 2. As the mitral annulus expands under pulsatile flow the SRSA expands with it, by ~17mm and contracts to its initial dimension as shown in Figure S13. This illustrates the conformability of SRSA within the left atrium and its ability to make contact with the atrial tissue under dynamic flow conditions. Furthermore, as seen from the videos, SRSA does not occlude blood flow.

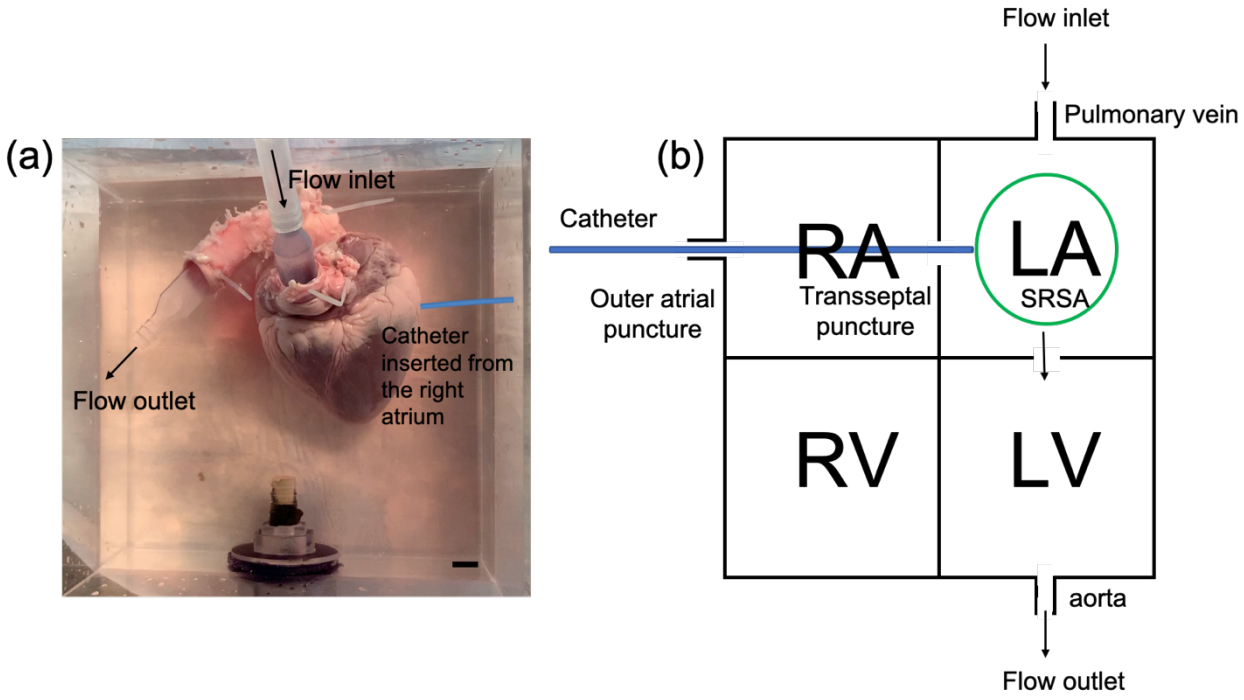

Figure S12. (a) Flow loop experimental setup using pulsatile flow on an excised porcine heart to evaluate conformability of SRSA. (b) The catheter position in relation to fluid flow is shown. The flow from the pump enters through one of the pulmonary veins and the flow leaves the heart from the aorta. The catheter is inserted from the right atrium through the transseptal wall into the left atrium. Scale bar is 1cm. Photo Credit: Alexandre Caprio, Weill Cornell Medicine

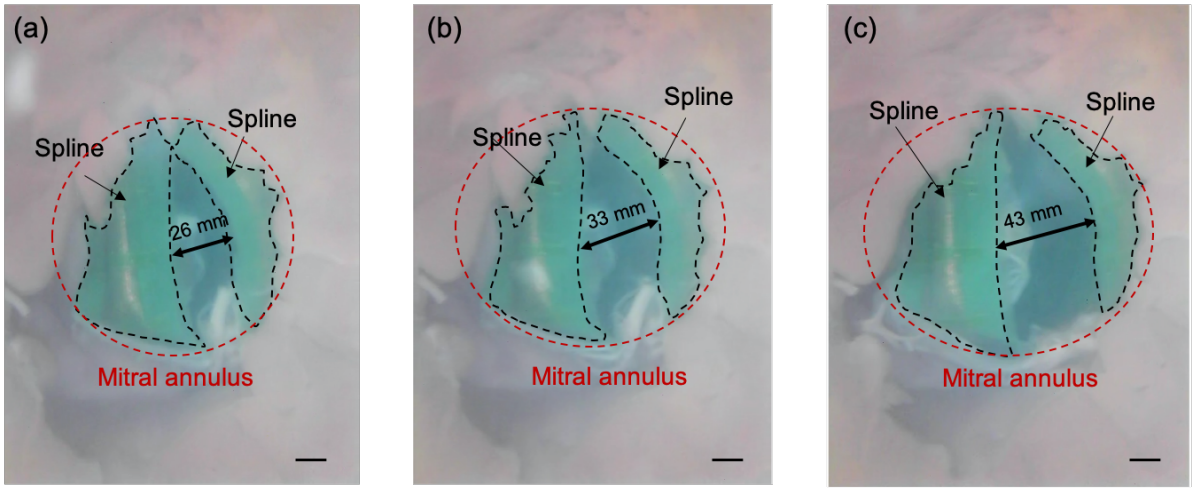

Diameter of the mitral annulus 103.8 mm

Diameter of the mitral annulus 111.9 mm

Diameter of the mitral annulus 120.9 mm

Figure S13. Conformability of SRSA to the atrial tissue during atrial motion. Splines of SRSA conform to the tissue surface as the mitral annulus expands under pulsatile flow. Scale bar is 1 cm. Photo Credit: Alexandre Caprio, Weill Cornell Medicine

Deflection and blocked force measurements

In order to characterize SRSA further, we conducted deflection and blocking force measurements. The importance of the fabrication procedure highlighted in this study is highlighted in Figure S14. As shown in the figure, direct integration of sensor arrays to the proposed actuator dramatically reduces the conformability of these actuators, thereby preventing them from being used in this application. The combination of the aforementioned fabrication techniques mentioned in this study and the novel laser postprocessing technique allow for retention of deflection in these actuators. We conducted blocked force experiments as proposed by Mac Murry et al (*43*) and Argiolas et al (*44*). The experimental setup is shown in Figure S13. Very small blocked force value was obtained of ~0.002 N for a pressure of 10PSI for a single actuator.

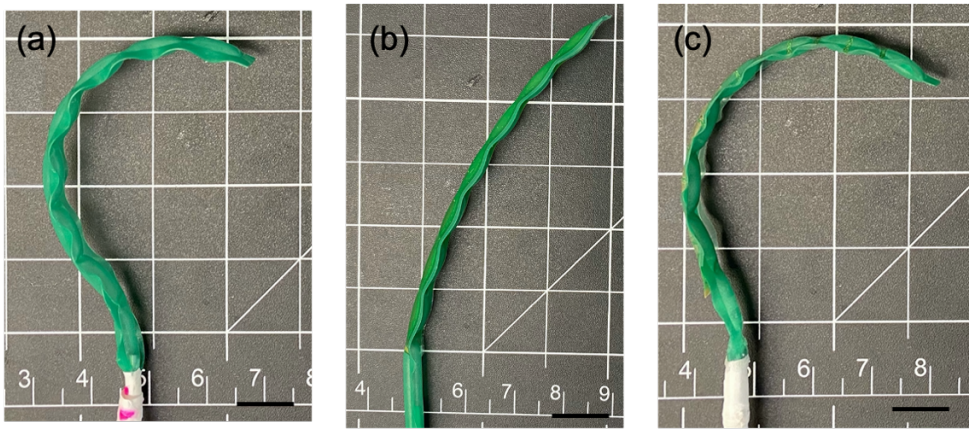

Figure S14. Deflection of SRSA with and without post processing. The conformability of SRSA is dependent on laser post-processing. Scale bar is 1cm. Photo Credits: Varun Kashyap, Weill Cornell Medicine

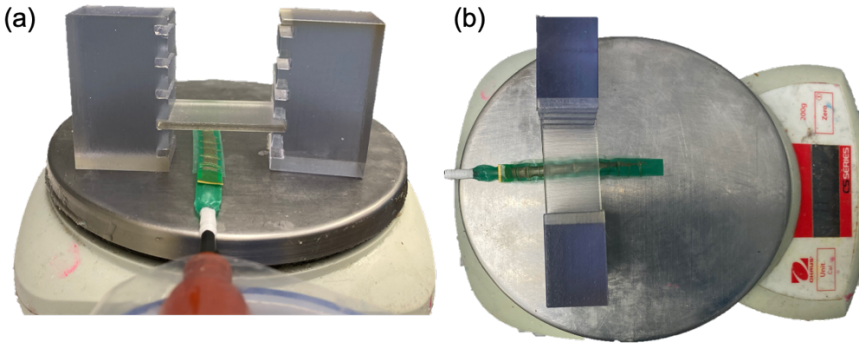

Figure S15. Experimental setup for blocked force measurements. Photo Credits: Varun Kashyap, Weill Cornell Medicine

Durability analysis

In order to confirm long term conformability, we conducted deflection experiments on the beam. We measured deflection of the beam on a calibrated cutting mat for every 10 actuations, upto 100 actuations as shown in Figure S16. The change in deflection was monitored as this directly corresponds to conformability of SRSA within the left atrium. As seen from the figure, the deflection of SRSA remains constant after 100 actuations, thereby proving their long-term conformability.

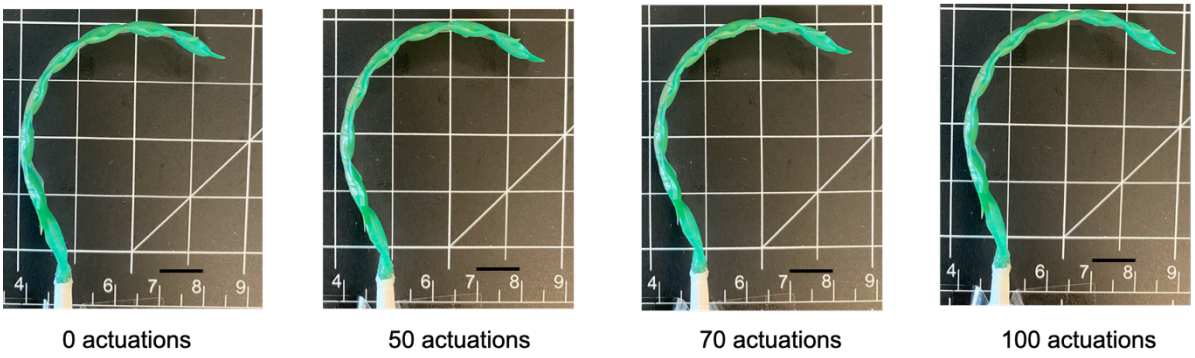

Figure S16. Evaluation of conformability for multiple actuations using deflection analysis. Scale bar is 1 cm. Photo Credit: Varun Kashyap, Weill Cornell Medicine

Micro CT conformability repeatability

We took two additional micro CT images for SRSA deployed in Atrium 1, which was the atrium with highest conformability in our initial analysis. The percentage conformability for near field measurements is shown in Figure S17. These values are comparable to those obtained during our initial analysis, thereby confirming repeatability of these conformability measurements.

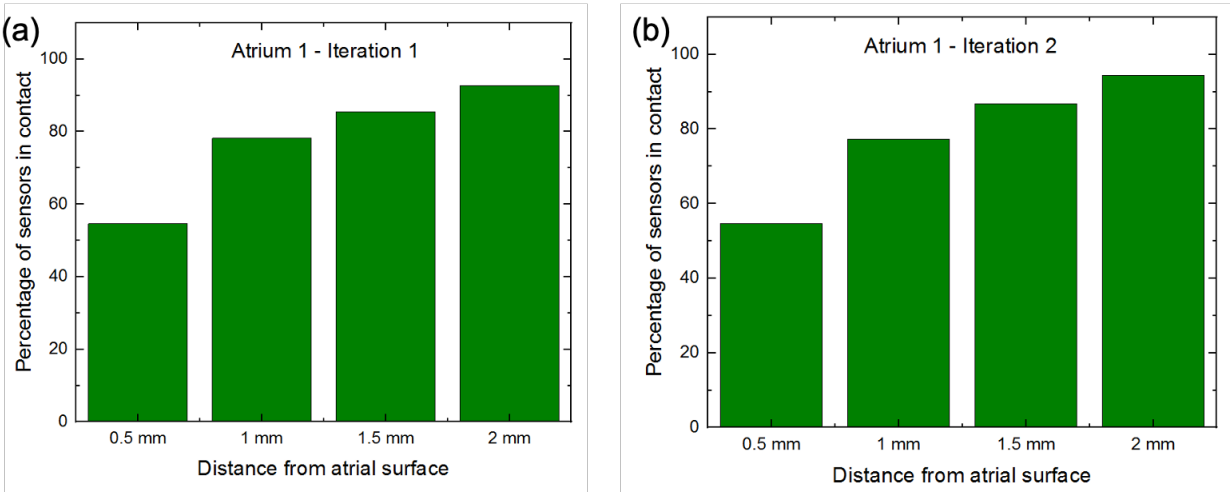

Figure S17: Repeatability of conformability experiments for atrium 1.

Electrode electroplating

We electroplated our electrodes with gold and palladium. The aforementioned procedure was followed to pass waveforms through a gelatin phantom atrial tissue. We characterized the ability of individual sensors to resolve features of the wave as shown in figure S18. We did not see a significant difference in the ability of the electrodes for mapping.

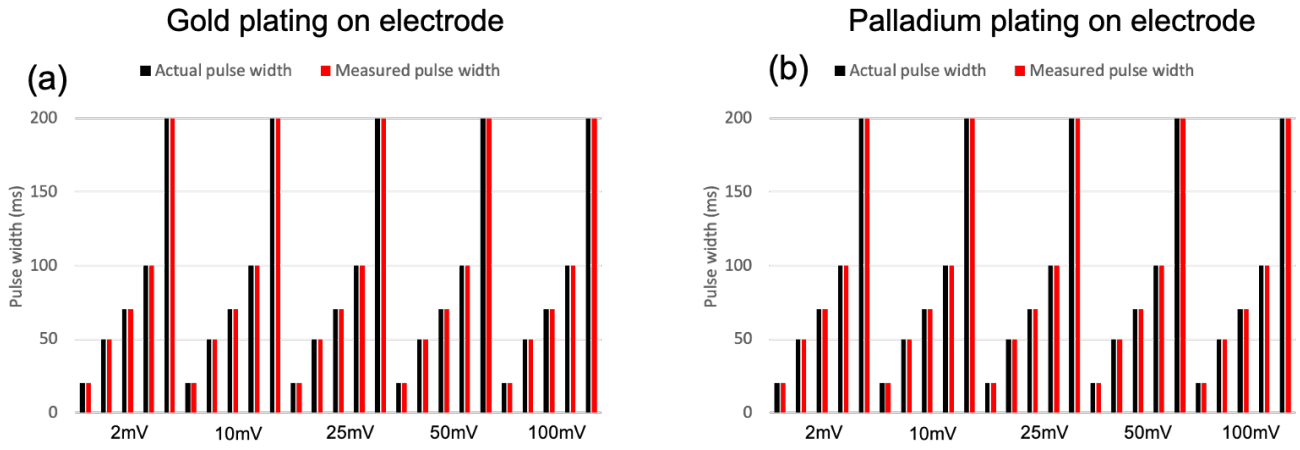

Figure S18. Performance of gold and palladium plated electrodes.

SRSA delivery through a mock full-length sheath

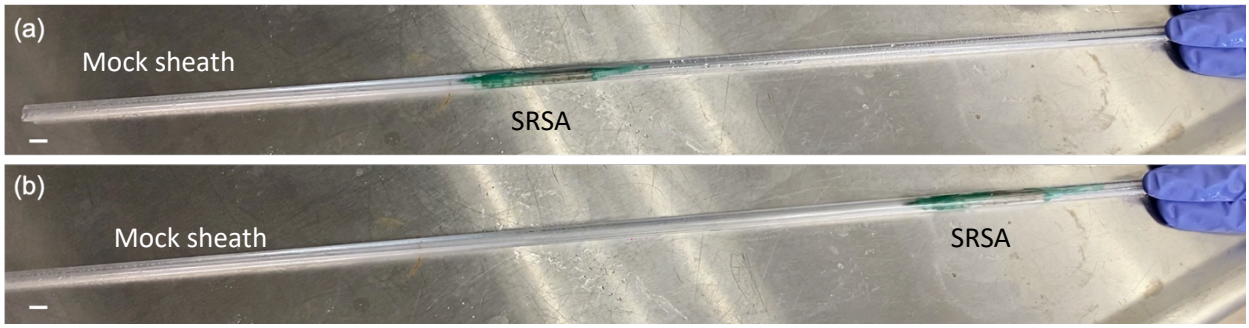

Figure S19. SRSA delivery through a mock full-length sheath. (a) catheter advanced through the sheath. (b) catheter retracted back. Scale bar is 1cm. Photo Credit: Varun Kashyap, Weill Cornell Medicine

Sensor characterization for multiple splines

In order to demonstrate performance of sensors on multiple splines of SRSA, the device was actuated on a gelatine based cardiac tissue phantom as described earlier in Figure S9. The phantom provides tissue-like electromagnetic and mechanical properties. A waveform with physiologically relevant voltage amplitude and frequency was passed through the phantom model using a function generator. Note that the control signal has a pulse width of 50 ms. Signals from 64 sensors spread over multiple splines were collected using an oscilloscope. Note that the values are averaged over 64 sensors. A representative parameter (ex. pulse width) from the collected signals was plotted as shown in Figure S20. All the sensors on individual splines are capable of resolving waveform characteristics for physiologically relevant voltage amplitude and frequency ranges accurately.

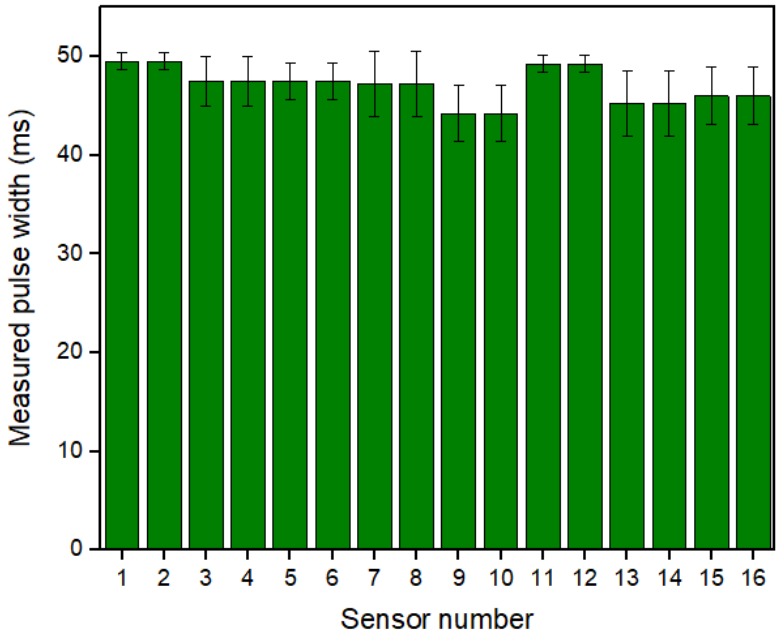

Figure S20. Measured pulse width averaged over 64 sensors (on multiple splines of SRSA) is plotted. Note that the control signal has a pulse width of 50ms. This shows the ability of SRSA sensors to resolve waveform characteristics for physiologically relevant voltage amplitude and frequency ranges accurately.

Supplementary Movies

Movie S1. Flow loop setup to evaluate conformability using an excised porcine heart

Movie S2. Conformability of SRSA within an excised porcine heart